Nonequilibrium Green's Function Model for Simulation of Quantum Cascade Laser Devices Under Operating Conditions

Andreas Wacker, Martin Lindskog, and David O. Winge

(Invited Paper)

***Abstract*—A simulation scheme based on nonequilibrium Green's functions for biased periodic semiconductor heterostructure devices is presented in detail. The implementation can determine current and optical gain both for small and large optical fields. Specific results for superlattices, quantum cascade lasers, and quantum cascade detectors are shown which demonstrate the capabilities of the approach.**

***Index Terms*—Nonequilibrium Green's functions (NEGF), quantum cascade laser, simulation.**

I. Introduction

QUANTUM cascade lasers (QCLs) [1] have become an important source of radiation for infrared spectroscopy [2]–[4]. In addition, lasing in the terahertz range [5] opens up a wide range of further applications [6]–[10]. These devices rely on a precise design of the underlying semiconductor heterostructure, so that the combination of electron tunneling and scattering provides inversion in the population of the subbands. While a first idea about the operation can be obtained by relatively simple principles such as level alignments and scattering rates [1], a full understanding of the operating requires a more detailed quantum description.

Typically the operation of QCLs is modeled by *rate equations* [11] between the levels of the active regions, while the current flow through the injector is taken into account phenomenologically. The transition rates are evaluated microscopically within Fermi's golden rule for phonon scattering [12], [13] and partially for electron–electron scattering [14], [15]. In addition, confined phonon modes [16] and hot phonon effects [17] have been studied. If one includes the injector states in such a simulation, one obtains a self-consistent simulation of the entire structure [18], [19] within the semiclassical carrier dynamics.

While rate equations only take into account the electron density of subbands, *Monte Carlo simulations* of the Boltzmann equation [20], [21] allow for a study of nonequilibrium distributions within the subbands [22]. Here, the importance of electron–electron scattering [23] is debated. In [24], Iotti and Rossi show that the impact of electron–electron scattering is strong if no elastic scattering mechanism is taken into account. In contrast the authors of [25] find that elastic impurity scattering gives stronger effects than electron–electron scattering.

Density matrices include the correlations $\rho_{\alpha\beta}$ between different quantum states $\alpha \neq \beta$. These are of particular importance for the tunneling through the injection barrier, where their neglect provides the wrong result, that is the peak tunnel current does not drop with the barrier width [26], [27]. In a more phenomenological way, this can be done on the level of densities [28]–[30], which is very cost effective. Taking into account the k-resolution, the equations for the density matrix $\rho_{\alpha\beta}(k_x, k_y)$ become much more involved [24], [27], [31]. Here, it is a well-known problem that unphysical negative occupations may occur in frequently used approximation schemes; see [27] for a thorough discussion. A possible solution by using further approximations is outlined in [32] on the level of densities.

Nonequilibrium Green's functions (NEGF) constitute a higher step of sophistication. They can be viewed as energy-resolved density matrices and allow for a consistent perturbative treatment of scattering and quantum evolution. On the other side, their numerical implementation is heavy, in particular if electron–electron scattering is considered. They have been used for QCL simulations by various groups in different types of implementations [33]–[38].

The purpose of this paper is to present a detailed account of our implementation of NEGF in Section II. On the one hand, this complements earlier descriptions [34], [35] for the stationary transport. Furthermore, we present our extension to include the lasing field beyond linear response, which we recently applied in [39]. We demonstrate the strength of the simulation tool by applications for superlattices, QCLs, and quantum cascade detectors (QCDs) in Sections III–V, respectively.

Manuscript received December 3, 2012; revised January 9, 2013; accepted January 9, 2013. Date of publication January 18, 2013; date of current version May 13, 2013. This work was supported by the Swedish Research Council.

The authors are with the Division of Mathematical Physics, Lund University, Lund 22100, Sweden (e-mail: andreas.wacker@fysik.lu.se; martin.lindskog@teorfys.lu.se; david.winge@teorfys.lu.se).

Color versions of one or more of the figures in this paper are available online at http://ieeexplore.ieee.org.

Digital Object Identifier 10.1109/JSTQE.2013.2239613

II. Theoretical Formulation

We consider a general sequence of heterostructure layers, where z is the growth direction. For an ideal structure, the system is translational invariant in the x and y directions and we use a

complete set of states

$$\Psi_{\alpha,\mathbf{k}}(x,y,z)=\varphi_\alpha(z)\frac{\mathrm{e}^{\mathrm{i}(k_x x+k_y y)}}{\sqrt{A}} \tag{1}$$

where $\mathbf{k}=(k_x,k_y)$ is a vector within the x,y plane of normalization area A. The states $\varphi_\alpha(z)$ can be chosen in different ways. Typical examples are eigenstates of the pure Hamiltonian $\hat{H}_0$ (also called Wannier–Stark states) as used by most groups, or a site representation as used in [37] and [38]. We usually apply Wannier States; see [34, Appendix A], which allow for a consistent description of periodic extended structures. In particular, their construction does not require any artificial boundary conditions (such as the Wannier–Stark states) and they provide reliable energy levels (while these energies are approximate in a site representation with a manageable number of grid points). Nevertheless, the following description can be used for any kind of orthonormal states $\varphi_\alpha(z)$.

With in this basis, the total Hamiltonian can be written as follows:

$$\hat{H}=\hat{H}_0+\hat{H}_{\mathrm{ac}}(t)+\hat{H}_{\mathrm{MF}}(t)+\hat{H}_{\mathrm{scatt}}. \tag{2}$$

Here, $\hat{H}_0$ contains the kinetic energy, the heterostructure potential, and the constant electric field F due to the applied bias.

$\hat{H}_{\mathrm{ac}}(t)$ is due to a laser field with the electrical component $F_{\mathrm{ac}}\vec{e}_z\cos(\omega t-kx)$. Here, $k=\sqrt{\epsilon_r}\omega/c$ with the refractive index $\sqrt{\epsilon_r}$. Neglecting terms of order k (just as in the common dipole approximation), we obtain the potentials [33]

$$\text{Coulomb gauge}\quad \vec{A}(t)=-\frac{F_{\mathrm{ac}}}{\omega}\vec{e}_z\sin(\omega t)\quad \phi(z,t)=0$$

$$\text{Lorenz gauge}\quad \phi(z,t)=-F_{\mathrm{ac}}z\cos(\omega t)\quad \vec{A}(t)=0$$

which allow us to construct $\hat{H}_{\mathrm{ac}}(t)$ in the standard way.

$\hat{H}_{\mathrm{MF}}(t)$ is the mean field due to the charge distribution $\rho(z,t)$ in the heterostructure, which is obtained by solving Poisson's equation. (Its time-independent part is frequently incorporated into $\hat{H}_0$.) Finally, $\hat{H}_{\mathrm{scatt}}$ describes the interaction with impurities, phonons, and other sources destroying the translational invariance in x and y directions. Thus, this term is not diagonal in $\mathbf{k}$, in contrast to all other contributions to $\hat{H}$.

Most physical observables can be expressed by the (reduced) density matrix

$$\rho_{\alpha\beta}(\mathbf{k},t)=\left\langle a^\dagger_{\beta\mathbf{k}}(t)a_{\alpha\mathbf{k}}(t)\right\rangle=\mathrm{Tr}\left\{\hat{\rho}a^\dagger_{\beta\mathbf{k}}(t)a_{\alpha\mathbf{k}}(t)\right\} \tag{3}$$

where the creation/annihilation operators $a^\dagger_{\alpha\mathbf{k}}(t)/a_{\alpha\mathbf{k}}(t)$ of the single particle level $\Psi_{\alpha\mathbf{k}}(x,y,z)$ have a time dependence in the Heisenberg picture and $\hat{\rho}$ is the density operator. Note that averaging over impurity positions and phonon mode occupations typically renders zero expectation values of $\langle a^\dagger_{\beta\mathbf{k}'}(t)a_{\alpha\mathbf{k}}(t)\rangle$ for $\mathbf{k}'\neq\mathbf{k}$. These density matrices $\rho_{\alpha\beta}(\mathbf{k},t)$ allow for the calculation of the relevant physical properties. For example, the electron sheet density in level α is given by $n_\alpha(t)=\bar{\rho}_{\alpha\alpha}(t)$, where

$$\bar{\rho}_{\alpha\beta}(t)=\frac{2}{A}\sum_{\mathbf{k}}\rho_{\alpha\beta}(\mathbf{k},t) \tag{4}$$

sums over the lateral degrees of freedom and the spin. Even more important is the current density in the growth direction

$$\begin{aligned}J(z,t)&=e\Re\left\{\left\langle\frac{\hat{p}_z-eA_z(z,t)}{m_c(z)}\right\rangle\right\}\\&=\frac{e}{\hbar}\sum_{\alpha,\beta}\left[\mathrm{i}W_{\beta\alpha}(z)-\frac{eA_z(z,t)d}{\hbar}F_{\beta\alpha}(z)\right]\bar{\rho}_{\alpha\beta}(t)\end{aligned} \tag{5}$$

where $A_z(z,t)$ is the z component of the electrodynamic vector potential (we tacitly assume that its x,y dependence is not of relevance), $e<0$ the charge of the electron, and

$$W_{\beta\alpha}(z)=-\frac{\hbar^2}{2m_c(z)}\left(\varphi^*_\beta(z)\frac{\partial\varphi_\alpha(z)}{\partial z}-\frac{\partial\varphi^*_\beta(z)}{\partial z}\varphi_\alpha(z)\right)$$

$$F_{\beta\alpha}(z)=\frac{\hbar^2}{d}\frac{\varphi^*_\beta(z)\varphi_\alpha(z)}{m_c(z)}.$$

In practice, $J(z,t)$ depends on the number of states used [40], as the completeness relation is not entirely satisfied for a finite basis. However, the spatial average over one period $J(t)$ converges much better and is used for almost all practical purposes. In the presence of an ac field with amplitude $F_{\mathrm{ac}}\cos(\omega t)$, we find a time-periodic current density

$$J(t)=\sum_h J_h\mathrm{e}^{-\mathrm{i}h\omega t}. \tag{6}$$

Here, J_0 is the dc current and the material gain can be obtained via the real part of the dynamical conductivity $\sigma(\omega)$ as

$$G(\omega)=-\frac{\Re\{\sigma(\omega)\}}{c\epsilon_0\sqrt{\epsilon_r}}=-\frac{1}{c\epsilon_0\sqrt{\epsilon_r}}\frac{J_1+J_{-1}}{F_{\mathrm{ac}}}. \tag{7}$$

Thus, the main task is to evaluate the density matrix $\rho_{\alpha\beta}(\mathbf{k},t)$ in the presence of Hamiltonian (2). (In fact, for most purposes it is sufficient to consider $\bar{\rho}_{\alpha\beta}(t)$ as used in many recent density matrix approaches [28]–[30], [32]). In this context, it is a major problem that a standard perturbative treatment of the scattering Hamiltonian(see [24] and [27]) provides negative densities, which is a general feature [41]. An outcome is to modify the scattering terms in a clever way; see, e.g., [32]. However, such an artificial procedure might mask relevant physical effects, where details of the *k*-distribution matter [38]. Thus, it is of general interest to have a formalism at hand, which is entirely based on a systematic treatment of perturbation theory and avoids unphysical outcomes. This justifies the far more evolved method of NEGF as discussed here.

A. Green's Functions

The formalism of NEGF [42]–[44] can be based on the following Green's functions: the correlation function (or "lesser"

Green's function)

$$G^{<}_{\alpha_1,\alpha_2}(\mathbf{k};t_1,t_2) = \mathrm{i}\langle \hat{a}^{\dagger}_{\alpha_2}(\mathbf{k},t_2)\hat{a}_{\alpha_1}(\mathbf{k},t_1)\rangle \tag{8}$$

which can be regarded as an extension of the density matrix (3) to different times, as well as the retarded and advanced Green functions

$$\begin{aligned} G^{\mathrm{r}}_{\alpha_1,\alpha_2}(\mathbf{k};t_1,t_2) &= -\mathrm{i}\Theta(t_1-t_2)\left\langle\left\{\hat{a}_{\alpha_1}(\mathbf{k},t_1),\hat{a}^{\dagger}_{\alpha_2}(\mathbf{k},t_2)\right\}\right\rangle \\ G^{\mathrm{a}}_{\alpha_1,\alpha_2}(\mathbf{k};t_1,t_2) &= \mathrm{i}\Theta(t_2-t_1)\left\langle\left\{\hat{a}_{\alpha_1}(\mathbf{k},t_1),\hat{a}^{\dagger}_{\alpha_2}(\mathbf{k},t_2)\right\}\right\rangle \\ &= \left[G^{\mathrm{r}}_{\alpha_2,\alpha_1}(\mathbf{k},t_2,t_1)\right]^{*} \end{aligned} \tag{9}$$

where $\{\hat{A},\hat{B}\} = \hat{A}\hat{B}+\hat{B}\hat{A}$ is the anticommutator. Using matrix notation, where matrices like $G_{\alpha\beta}$ are denoted by bold capitals $\mathbf{G}$, differentiating in time provides the equations of motion

$$\begin{aligned} &\left(\mathrm{i}\hbar\frac{\partial}{\partial t_1} - E_k\right)\mathbf{G}^{\mathrm{r/a}}(\mathbf{k};t_1,t_2) - \mathbf{U}(t_1)\mathbf{G}^{\mathrm{r/a}}(\mathbf{k};t_1,t_2) \\ &\quad = \hbar\delta(t_1-t_2)\mathbf{1} + \int\frac{\mathrm{d}t}{\hbar}\mathbf{\Sigma}^{\mathrm{r/a}}(\mathbf{k};t_1,t)\mathbf{G}^{\mathrm{r/a}}(\mathbf{k};t,t_2) \end{aligned} \tag{10}$$

where the matrix $\mathbf{U}$ refers to the k-diagonal part of the Hamiltonian

$$\hat{H}_0 + \hat{H}_{\mathrm{ac}}(t) + \hat{H}_{\mathrm{MF}}(t) = \sum_{\alpha,\beta,\mathbf{k}} U_{\alpha,\beta}(\mathbf{k},t)a^{\dagger}_{\alpha}(\mathbf{k})a_{\beta}(\mathbf{k}) \tag{11}$$

and $E_k = \hbar^2\mathbf{k}^2/2m^*$ is the in-plane energy, where we use the effective mass m^* of the well for simplicity. (Nonparabolicity has been recently considered in the Green's function model of [45].) The self-energies $\mathbf{\Sigma}$ take into account $\hat{H}_{\mathrm{scatt}}$ perturbatively. A similar equation of motion for the lesser Green's function is solved by the Keldysh relation [44]

$$\begin{aligned} &\mathbf{G}^{<}(\mathbf{k};t_1,t_2) \\ &\quad = \int\frac{\mathrm{d}t}{\hbar}\int\frac{\mathrm{d}t'}{\hbar}\mathbf{G}^{\mathrm{r}}(\mathbf{k};t_1,t)\Sigma^{<}(\mathbf{k};t,t')\mathbf{G}^{\mathrm{a}}(\mathbf{k};t',t_2). \end{aligned} \tag{12}$$

In earlier work [34], [35], we focused on the stationary behavior, where the Green's functions only depend on the time difference $t_1 - t_2$. Now, we consider a periodic solution, where the system is allowed to oscillate at a frequency ω and its higher harmonics as a consequence of the time periodicity of $\hat{H}_{\mathrm{ac}}(t)$ (and consequently $\hat{H}_{\mathrm{MF}}(t)$). Setting

$$\mathbf{U}(t) = \sum_h \mathbf{U}_h e^{-\mathrm{i}h\omega t} \tag{13}$$

and using the Fourier decomposition similar to [66]

$$F(\mathbf{k};t_1,t_2) = \frac{1}{2\pi}\int \mathrm{d}E\sum_h \mathrm{e}^{-\mathrm{i}E(t_1-t_2)/\hbar}F_h(\mathbf{k},E)\mathrm{e}^{-\mathrm{i}h\omega t_1} \tag{14}$$

both for self-energies and Green's functions, we find the Dyson equation

$$\begin{aligned} \mathbf{1}\delta_{h,0} &= (E+h\hbar\omega-E_k)\mathbf{G}^{\mathrm{r/a}}_h(\mathbf{k},E) \\ &\quad - \sum_l\left(\mathbf{U}_{h-l} + \Sigma^{\mathrm{r/a}}_{h-l}(\mathbf{k},E+l\hbar\omega)\right)\mathbf{G}^{\mathrm{r/a}}_l(\mathbf{k},E) \end{aligned} \tag{15}$$

and the Keldysh relation

$$\begin{aligned} \mathbf{G}^{<}_h(\mathbf{k},E) &= \sum_{l,l'}\mathbf{G}^{\mathrm{r}}_{h-l-l'}(\mathbf{k},E+(l+l')\hbar\omega) \\ &\quad \times \Sigma^{<}_{l'}(\mathbf{k},E+l\hbar\omega)\mathbf{G}^{\mathrm{a}}_l(\mathbf{k},E) \end{aligned} \tag{16}$$

providing a set of equations to determine the Green's functions for given self-energies within the truncation $|h| \le h_{\max}$. The density matrix is then element wise reproduced by

$$\rho_{\alpha\beta}(\mathbf{k},t) = -\mathrm{i}\int\frac{\mathrm{d}E}{2\pi}\sum_h G^{<}_{\alpha\beta,h}(\mathbf{k},E)\mathrm{e}^{-\mathrm{i}h\omega t} \tag{17}$$

allowing for the evaluation of current and gain as outlined previously.

B. Self-Energies

For the self-energies, we use the self-consistent Born approximation. In Appendix B, details on the scattering processes are given. Here, we restrict to the main concept. For example, for elastic scattering

$$\hat{H}^{\mathrm{elast}}_{\mathrm{scatt}} = \sum_{\alpha\mathbf{k}\beta\mathbf{k}'} V_{\alpha\beta}(\mathbf{k}-\mathbf{k}')a^{\dagger}_{\alpha\mathbf{k}}a_{\beta\mathbf{k}'} \tag{18}$$

we have

$$\Sigma^{</\mathrm{r}}_{\alpha\alpha',h}(E,\mathbf{k}) = \sum_{\beta\beta',\mathbf{k}'}\langle V_{\alpha\beta}(\mathbf{k}-\mathbf{k}')V_{\beta'\alpha'}(\mathbf{k}'-\mathbf{k})\rangle\, G^{</\mathrm{r}}_{\beta\beta',h}(E,\mathbf{k}') \tag{19}$$

where $\langle\rangle$ averages over different realizations of the scattering potential, which restores the spatial homogeneity. For the same reason, the Green's function and self-energy do only depend on the absolute value $|\mathbf{k}|$, which is conveniently expressed by E_k. Then, (19) can be rewritten as

$$\Sigma^{</\mathrm{r}}_{\alpha\alpha',h}(E,E_k) = \sum_{\beta\beta'}\int_0^{\infty}\mathrm{d}E_{k'}\,X_{\alpha\alpha',\beta\beta'}(E_k,E_{k'})G^{</\mathrm{r}}_{\beta\beta',h}(E,E_{k'}). \tag{20}$$

Assuming that $G^{</\mathrm{r}}_{\beta\beta',h}(E,E_{k'})$ peaks at $E_{k'}\approx E-(E_\beta+E_{\beta'})/2 = E'_{\mathrm{typ}}$, and $\Sigma^{</\mathrm{r}}_{\alpha\alpha',h}(E,E_k)$ is mostly needed at $E_k \approx E-(E_\alpha+E_{\alpha'})/2 = E_{\mathrm{typ}}$, we may approximate $X_{\alpha\alpha',\beta\beta'}(E_k,E_{k'})$ by $X_{\alpha\alpha',\beta\beta'}(E_{\mathrm{typ}},E'_{\mathrm{typ}})$, which effectively corresponds to delta-like scattering potentials. Here, we usually chose the value of E such that $\mathrm{Min}\{E_{\mathrm{typ}},E'_{\mathrm{typ}}\} = 1\mathrm{meV}+0.3k_BT$. This *constant k approximation* provides an essential simplification of the numerics, as the self-energies do not depend any longer on $\mathbf{k}$.

The k-dependence of Σ has been shown to be of relevance for longitudinal optical phonon scattering [46], [47], so the results have to be taken with some care. However, with our choice of a level-dependent $E_{\mathrm{typ}},E'_{\mathrm{typ}}$, we obtained reasonable results for all cases studied so far. A comparison with an exact treatment of intersubband absorption for roughness scattering [48] showed that our approach reproduced the peak very well, but overestimated the absorption tails at high energies, where the momentum dependence of the matrix elements is crucial.

C. Boundary Conditions and Iteration Scheme

We consider a periodic system, where the same sequence of layers is repeated infinitely (d is the length of the period). We tacitly assume that the solution follows this periodicity.[1] Taking into account a potential drop eFd per period due to the external dc bias, this implies in Coulomb gauge

$$\Sigma_{\alpha\beta,h}(E) = \Sigma_{\alpha'\beta',h}(E + eFd)$$

if the states $\alpha'\beta'$ are shifted by one period with respect to $\alpha\beta$. (For the Lorenz gauge, the transformation is more complex and mixes terms with different h.) Thus, it is sufficient to evaluate the self-energies $\Sigma_{\alpha\beta,h}(E)$, where the state α is located in a given central period.

In order to obtain a solution, we determine $G^{\mathrm{r/a}}$ by solving (15) for a given $\Sigma_{\alpha\beta,h}(E)$ taking into account the states of the central period as well as N_{per} periods on either side. Then, we determine $G^{<}$ via (16). Based on these Green's functions, we calculate the new self-energies $\Sigma_{\alpha\beta,h}(E)$ for α being located in the central period. If the new self-energies do not agree with the starting ones, we choose new values by the Broyden algorithm [49] and repeat the iteration. Convergence with an accuracy of typically 5×10^{-4} (or even smaller) is obtained after 30–100 iterations. Finally, the quantities of interest are evaluated from the Green's functions in the central region. By increasing $h_{\max}$ and N_{per}, the quality of the respective truncations can be verified.

D. Meanfield

The electron charge density $\rho_{el}(z,t)$ is directly obtained from the density matrix. Solving Possion's equation together with the doping density for periodic boundary conditions $\phi(z) = \phi(z + d)$ provides the potential $\phi(z,t)$, which determines $\hat{H}_{\mathrm{MF}}(t)$.

III. Comparison with Analytical Results for Superlattices

Semiconductor superlattices represent the simplest periodic structures and provide an excellent testing ground for the code. Here, we consider the structure of [50], which has a rather large miniband width $\Delta = 26.4$ meV. Fig. 1(a) shows the calculated current-bias relation using the nominal system parameters and neglecting interface roughness (which should be small, as wells and barriers are binary systems and carefully chosen to consist of an integer number of monolayers). All calculations are done at a lattice temperature of 300 K and we use $N_{\mathrm{per}} = 3$. The peak height and position agree reasonably well with the measured characteristics. The data can be fitted very well by a simple expression $J(F) = 2J_{\max} eFd\Gamma/((eFd)^2 + \Gamma^2)$ based on the Esaki–Tsu characteristics [51] where $\Gamma = 18$ meV is the average scattering rate multiplied by $\hbar$. This is expected, as the miniband model is good for $\Delta \gtrsim \Gamma$ and $\Delta \gtrsim |eFd|$ [52]. Indeed, minor deviations are seen for larger bias drops Fd per period. Following the work of [53], analytical expressions can be obtained within the Esaki–Tsu model even for a finite ac field (see [54, Section VI.2] for details), which can be used for comparison.

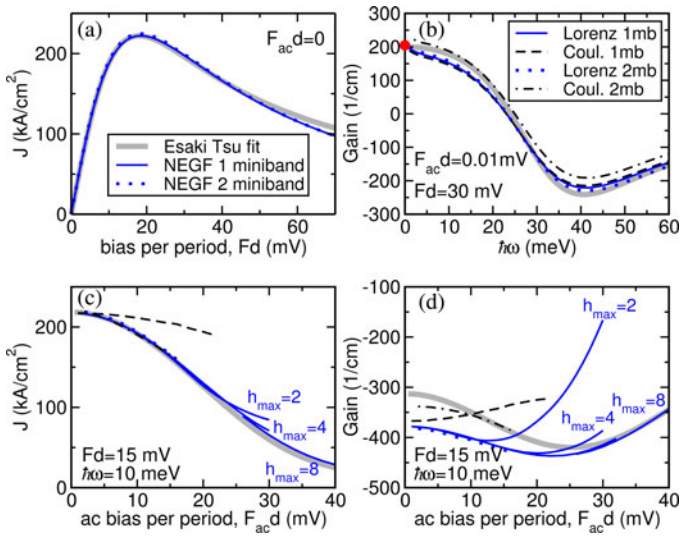

Fig. 1. Results of the NEGF simulation for the superlattice of [50]. The thick gray line gives the analytic solution of the simplified miniband model for comparison. The NEGF solutions are displayed for one miniband (mb) (full/dashed line) and two minibands (dotted/dash–dotted line) for Lorenz/Coulomb gauge, respectively. In panels (c) and (d), different choices of $h_{\max}$ are shown for Lorenz gauge and one miniband, while all other curves are solutions with sufficiently high $h_{\max}$. In panel (b), the gain value at $\omega \to 0$ obtained from the NEGF conductance in panel (a) is marked by a dot.

In Fig. 1(b) the gain is shown for a weak ac field at a dc bias dropping over one period of $Fd = 30$ mV. Here, we are in the region of negative differential conductivity of the superlattice, and consequently, gain occurs for $\hbar\omega \lesssim |eFd|$. The NEGF solutions are in reasonable agreement with the simple model, which can be seen as a validation for both approaches. We note that the choice of gauge does not affect the result much. However, it can be seen that the inclusion of the second subband (i.e., letting α run over two states per well) changes the result slightly for the Coulomb gauge. (The current–voltage characteristics are not affected as the second miniband, located 300 meV above the first miniband, is essentially empty.) Finally, we see that the gain approaches the value $G_0 = -\frac{\sigma_{\mathrm{dc}}}{c\epsilon_0\sqrt{\epsilon_r}} = 205$/cm for $\omega \to 0$, where the dc conductivity σ_{dc} is obtained from the slope of the current–voltage characteristics.

Fig. 1(c) shows the dc current at $Fd = 15$ mV as a function of the ac-field strength. We find that the current drops as a result of dynamical localization [55]. The result in Lorenz gauge and the analytic miniband model agree very well. For the Coulomb gauge, the agreement is only good if two minibands are taken into account. For the Lorenz gauge, we have shown simulations with different numbers $h_{\max}$. As expected, with increasing $eF_{\mathrm{ac}}d$ a larger number of h-components is needed in order to reach convergence.

Finally, Fig. 1(d) shows the gain for $\hbar\omega = 10$ meV at a dc bias of $Fd = 15$ mV as a function of the ac-field strength. The behavior is less dramatic. Here, the agreement between the NEGF solution and the analytic miniband model is only of qualitative

[1] Recently nonperiodic solutions have been discussed in [65]. As this effect appears in direct connection to the injecting contact, it is not clear whether this is of relevance far inside the periodic structure.

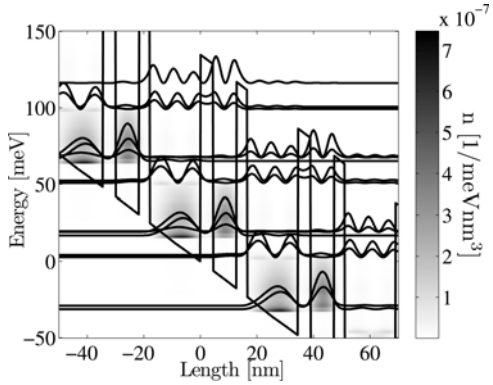

Fig. 2. Energetically and spatially resolved electron density $\rho(E,z)$ and the Wannier–Stark states of the QCL in [56] for a bias drop per period $Fd = 48.25$ mV.

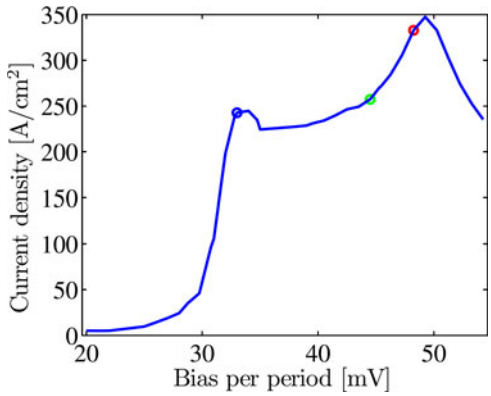

Fig. 3. Current-bias relation for the QCL in [56]. The circles mark the operating points where the gain is simulated and the conductivity is calculated.

nature. A better agreement would be surprising, as the high fields $F + F_{\rm ac}$ in combination with the high frequency ω are limiting the validity of the miniband model. The disagreement between the gauges is stronger and again, the result in Coulomb gauge depends on the number of minibands included.

These findings indicate that the NEGF model provides reasonable results in Lorenz gauge. In Coulomb gauge, the results depend strongly on the number of states included, even, if they are not directly involved. This may be attributed to the A_z term in the current (5). Technically, the equivalence between the two gauges requires the completeness relation for the basis used. For any finite basis, the completeness relation is only approximate, and thus, the equivalence between the approaches is not guaranteed. The data shown here indicate that the Lorenz gauge is more reliable.

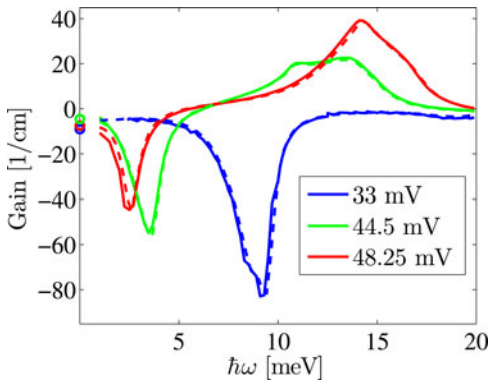

Fig. 4. Gain spectrum for $F_{\rm ac}d = 1$ mV at different biases for the QCL in [56] at two different gauges (solid lines: Lorenz; dashed lines: Coulomb). Circles mark the gain coefficients at $\omega \to 0$ calculated from the conductivity.

IV. QCL Results

A. Characterization of a QCL

In order to test the validity of our model, we present simulation results on the QCL structure of [56]. The structure is shown in Fig. 2, with the Wannier–Stark states and the energetically and spatially resolved electron density $\rho(E,z)$, directly found from the Green's function by

$$\rho(E,z) = \frac{2e}{2\pi {\rm i} A} \sum_{\mathbf{k}} \sum_{\alpha\beta} G^{<}_{\alpha\beta,h=0}(E,\mathbf{k}) \varphi^{*}_{\beta}(z)\varphi_{\alpha}(z). \quad (21)$$

Fig. 3 shows the current-bias relation without an external ac field at a lattice temperature of 50 K. The peak current $\sim$350 A/cm^2 is reached at 49 mV/period, which corresponds well with the experimentally observed peak at lasing at about 48 mV/period, where the current for a nonlasing device was measured to be $\sim$ 400 A/cm^2. The relatively large peak around 34 mV/period is of much smaller magnitude in the measurements. It corresponds to tunneling over two barriers. We think that dephasing is underestimated in our model here, probably due to the neglect of electron–electron scattering.

The simulated gain spectra for two gauges of a weak applied ac field are shown in Fig. 4. As discussed previously, the gauge transformations should in principle leave the results unchanged, but the incompleteness of the basis used gives rise to minor numerical differences. However, the results for different gauges agree fairly well for low ac bias as in the case for the superlattice discussed previously.

Again, we validate our model by comparing the theoretical value of the gain coefficients with the simulated gain spectra. In Fig. 4, the gain coefficients at $\omega \to 0$ are marked with circles. These have been calculated from the slope of the *IV* curve at the bias points indicated in Fig. 3 (using a quadratic fit) to be -9.09, -4.59, and -7.523/cm for increasing bias. The gain at low ω can be seen to approach the calculated values. Experimentally, lasing is observed at $\hbar\omega = 11.5$ and 13.3 meV at lower bias and at $\hbar\omega = 16$ meV for higher bias, which agrees well with our gain spectrum.

B. Integrated Absorption

The physics of gain in a QCL is essentially the physics of intersubband absorption and stimulated emission. The total absorption of all states in the conduction band, which we will here denote the integrated absorption, can be estimated

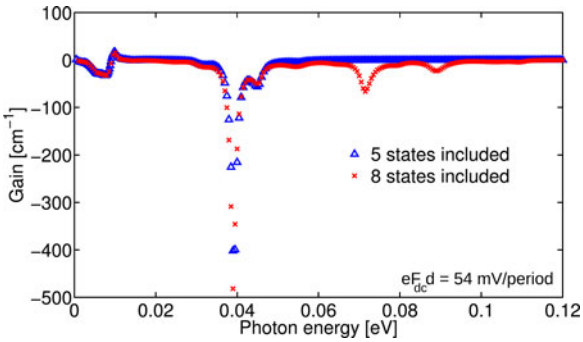

Fig. 5. Simulated absorption on a structure presented in [59]. Results from two different simulations are compared, one using 5 states per period and one using 8 states per period. As a reference, the conduction band offset in this structure is about 135 meV.

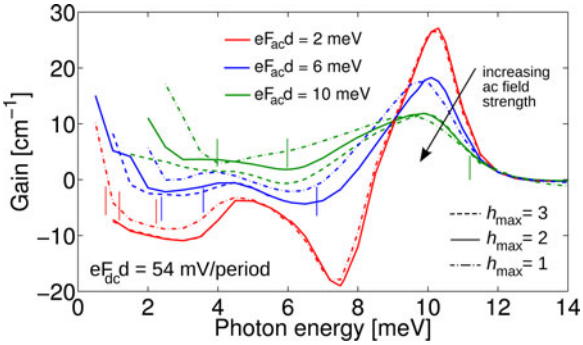

Fig. 6. Simulations with different $h_{\max}$ for three ac field strengths. An estimate of the critical frequency for each calculation is shown with a line.

following [57] and [58] to

$$\int_0^\infty d\omega\, \alpha_{\text{intersubband}}(\omega) = n_{\text{av}} \frac{\pi e^2}{2m^* c\epsilon_0 \sqrt{\epsilon_r}} \tag{22}$$

with $n_{av} = \sum_i n_i/d$ as the average 3-D carrier distribution and $\sqrt{\epsilon_r}$ again the refractive index. Note that this expression depends neither on the structure nor on the applied bias.

The constant property of the integrated absorption provides an excellent opportunity to test the model. To do this, we investigate a structure presented in [59]. This is a four-well QCL where the main transport properties can be retrieved from simulations by taking the first five states in each period into account. For this structure, simulations were carried out over a wide range of frequencies, and the results are shown in Fig. 5. The integrated absorptions for the two cases are found via numerical integration over the frequency interval to yield 2.23 eV/cm (1.62 eV/cm) when including 8 (5) states. Here, the errors in the numerical calculation can be severe as the number of points in the critical regions are few, and then exaggerated by the numerical integration. The simulated integrated absorption should be compared to the theoretical value of 2.41 eV/cm from (22).

As seen in the figure, the inclusion of states not contributing to transport is crucial in order to reproduce the correct integrated absorption. It is worth noting that the difference between a noncomplete basis set of five states and one almost complete of eight states is large. This shows again the importance of the completeness relation in the model, as we see here that an incomplete basis does not nearly reproduce the theoretically predicted result. The ninth state is in the continuum, and its importance is so far neglected.

Looking closer at (22), we note that the effective mass m^* is in fact z-dependent, as it is not the same in the barriers as in the wells. However, absorption will occur where the electrons are localized, as this is the argument for approximating the mass in these calculations with the effective mass of the wells of the heterostructure. Therefore, we expect the theoretical estimate to slightly overshoot the real value. Although the electrons are most probably found in one of the wells, we would find a certain percentage in the barriers, effectively raising the average mass and thus contributing to lower integrated absorption. This should also be taken into account when interpreting the results given previously.

C. High Intensity

Recently, we showed the relevance of nonlinear effects on the gain spectrum of a QCL [39]. In this context, it is important to study the convergence of the solution depending on the truncation parameter $h_{\max}$. Obviously, for low intensity of the ac field, a sharp truncation is very reasonable but when the photon energy is comparable to the ac field strength higher harmonics are needed in order to expand the space of allowed response functions of the system.

This criterion can be expressed as $eF_{\text{ac}}d \lesssim h_{\max}\hbar\omega$, for $N_{\text{per}} = 1$ used here. More orders of the response function must be taken into account when calculating with low photon energies $\hbar\omega$. This can be understood as including higher orders of absorption phenomena, as several photons of low energy can give the same absorption effect in the electronic system as one photon at the exact transition energy. These effects are naturally more important as intensity is increased.

The lowest truncation possible is $h_{\max} = 0$ which cannot treat any external light field at all but gives the stationary behavior of the system. Second lowest would then be $h_{\max} = 1$, where response at the fundamental frequency is seen. This gives the main part of the system dynamics, making it possible to retrieve quantities such as gain and absorption. Higher orders $h_{\max} > 1$ provide higher accuracy as more dynamical effects are taken into account as more Fourier components of the Green's function enter the system. This is important for low photon energies as discussed before. For terahertz QCLs, which operate at typical photon energies of 10 meV, large parts of the gain spectra are actually in the regime where the higher harmonics play an important role. In order to illustrate the importance, simulations of a QCL described in [59] are displayed in Fig. 6. The main effect, as discussed in detail in [39], is the reduction of gain with the intensity of the optical field due to bleaching.

The simulations show that it is not trivial to approach the low-frequency part of the spectra with a finite ac field strength. At the energy scale of the transport dynamics, the photon energies are now small, and a number of photons would be required in order to affect the system on the same premises as in the cases

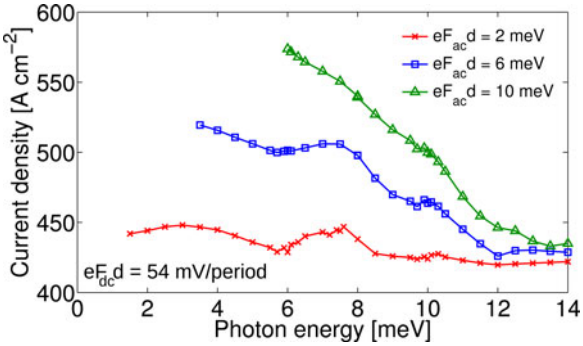

Fig. 7. Current at the same points as in Fig. 6 for $h_{\max} = 2$ plotted for the three different intensities. Data only taken at points where we estimate the simulations to be accurate.

of higher photon energy. This is why $h_{\max}$ is such an important parameter in the results shown in Fig. 6.

Here, the simulations with $h_{\max} = 3$ are the best cases and closest to the would-be exact calculation. For this system, it is on the limit of what is at the moment possible for us to do and only a few points are shown for the $h_{\max} = 3$ case, plotted as dashed lines in the figure. The simulations for different cases of $h_{\max}$ eventually coincide at higher photon energies as expected, early for low ac field strength and later for high ac field strength. It is clear from the results that the higher harmonics are of importance at operating intensities above $eF_{\rm ac}d = 6$ meV. In the plot we also show, for each ac field strength and $h_{\max}$, an estimation of the critical frequency. At this frequency, one should start being restrictive in trusting the results of the simulations.

In a QCL under operating conditions, the laser field will drive the current as the frequency of the photons is matched to the energy difference of the upper and lower laser state, stimulating emission and thus destroying the inversion of the carriers. This will result in a higher current through the system, and this can be seen in Fig. 7 where current is plotted at the same points as in Fig. 6 for $h_{\max} = 2$. The general trend is that for a given ac field strength the current increases with decreasing photon energies. This can be attributed to the fact that with decreasing photon energy, the number of photons increases for a fixed intensity. Therefore, more stimulated transitions occur, which provide extra channels for the electron transport.

Characteristic features can also be seen at the absorption peak at $\hbar\omega \sim 7$ meV and at the gain peak at $\hbar\omega \sim 10$ meV, compared with Fig. 6. We attribute the first peak in current to a redistribution of carriers from localized states to more mobile ones. At the gain peak at $\hbar\omega \sim 10$ meV, the stimulated emission provides an enhanced current along the common current path through the structure. This is commonly seen experimentally as a change of conductance at the onset of lasing.

Finally, above $\hbar\omega > 13$ meV, the current is hardly affected by the laser field. This is just the region without any significant absorption/gain, as can be seen in Fig. 5.

V. Quantum Cascade Detector

A suitable application of our model other than the QCL is the QCD [60], which is an alternative to the quantum well infrared photodetector (QWIP) for detecting infrared radiation. In contrast to the QWIP and many other photodetectors, the QCD operates at zero (or very small) bias, and therefore has minimal dark currents, in addition to having a narrow detection wavelength width.

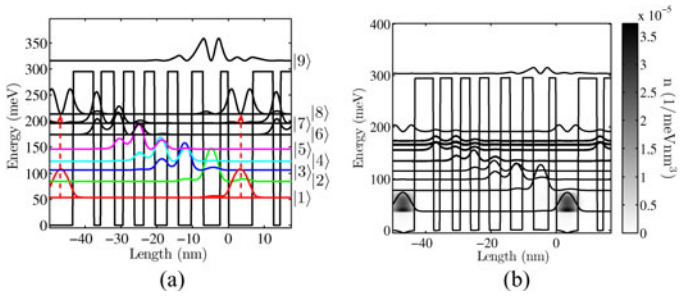

Fig. 8. (a) Basis states of the QCD, numbered from bottom to top. (b) Maxima of the density of states and the electron density.

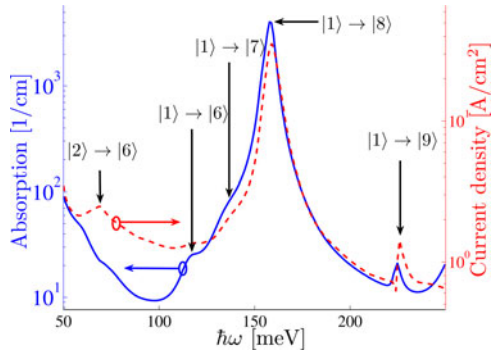

Fig. 9. Absorption (blue) and response current (red) as functions of the applied ac field frequency. The optical transitions causing the absorption and response peaks are indicated.

We will now study the QCD presented in [61], shown in Fig. 8(a) with the calculated basis states. In Fig. 8(b), we show the density of states (lines) at the energies where it has maxima. The reason for doing this is that the Wannier–Stark states, conventionally used as basis states that here contain mean field, are not defined at zero bias, and that the Wannier states do not include these effects. The density of states allows for determining which transitions are most probable with respect to populated and empty states.

Light is detected when an electron in the ground state of the widest, heavily doped well, $|1\rangle$, absorbs a photon with an energy matching the transition $|1\rangle \to |8\rangle$. The electron will thereby occupy state $|8\rangle$. Tunneling and scattering then allow for a cascading current from $|8\rangle$ down to the ground state of the neighboring period, to the right in Fig. 8. This gives an overall current flowing through the device (consisting of 50 periods or so) that is detected at the terminals.

Fig. 9 shows the simulated absorption and the response current arising from the photon-absorbing carriers. This current is a second-order effect, since it arises from carriers excited by the applied ac field. The main peaks are located at (going from low to high $\hbar\omega$) 69, 119, 138, 159, and 226 meV. Using the labeling in Fig. 8 (a) and taking the energy differences between the density of states maxima in Fig. 8 (b), the response peaks are

attributed to the transitions shown in Fig. 9. The QCD current response agrees almost exactly with the absorption peaks.

The experimentally measured QCD [61] showed the same structure for both absorption and response current as the presented simulations. The simulated peaks are shifted to higher frequencies by about 5 meV (more for larger transitions, and less for smaller transitions) with respect to the measured peaks. We attribute this to the neglect of nonparabolicity in our current scheme. In general, nonparabolicity reduces the energy of high energy states.

VI. Conclusion

We have presented our implementation of NEGF for the simulations of heterostructure devices in detail. Our model allows for a reliable determination of the current-field relation in most cases. However, some problems exist with extra peaks due to long range tunneling, which indicates that some dephasing channels are still missing. The main advance compared to previous implementations is the possibility to treat the radiation field even beyond linear response. This allows for studying a variety of important effects such as dynamical localization in superlattices, gain bleaching in quantum cascade lasers, and photon-assisted currents in QCDs. For small optical fields, the choice of the gauge does not matter much. However, the Coulomb gauge seems to require the inclusion of higher minibands in a superlattice even if they do not contribute explicitly. This effect is particularly strong for large optical fields.

Appendix A
Angle Averaged Scattering Matrix Elements

Using the self-consistent Born approximation in (19), we already argued for the use of only the absolute value $|\mathbf{k}|$ for the potentials. This means that when transforming the self-energies into a function of $E_k = \hbar^2\mathbf{k}^2/2m^*$ and $E_{k'}$ instead of $\mathbf{k}$ and $\mathbf{k}'$, we have to write the self-energy as

$$\Sigma^{</\mathrm{ret}}_{\alpha\alpha',h}(E,E_k) = \sum_{\beta\beta'}\int_0^\infty \mathrm{d}E_{k'}\frac{A}{(2\pi)^2}\frac{m^*}{\hbar^2} \times\int_0^{2\pi}\mathrm{d}\phi\langle V_{\alpha\beta}(E_k,E_{k'},\phi)V_{\beta'\alpha'}(E_k,E_{k'},\phi)\rangle \times G^{</\mathrm{ret}}_{\beta\beta',h}(E,E_{k'})$$

where we now have converted the sum over $\mathbf{k}'$ into a 2-D integral of E'_k and the angle $\phi = \angle(\mathbf{k},\mathbf{k}')$. Now, we identify the second-rank tensor $X_{\alpha\alpha',\beta\beta'}$ as the angle averaged part of the scattering matrix elements as a function of $E_k, E_{k'}$ in the following way:

$$\Sigma^{</\mathrm{r}}_{\alpha\alpha',h}(E,E_k) = \sum_{\beta\beta'}\int_0^\infty \mathrm{d}E_{k'}\,X_{\alpha\alpha',\beta\beta'}(E_k,E_{k'}) \times G^{</\mathrm{r}}_{\beta\beta',h}(E,E_{k'}) \quad (23)$$

where also the constants are included in $X_{\alpha\alpha',\beta\beta'}$. As discussed previously, these tensors are evaluated at certain typical energies E_{typ} and $E_{\mathrm{typ}'}$ which allow us to take the tensors outside the integral leaving an expression where we only need the k-integrated Green's function for the evaluation of the self-energies.

Appendix B
Details for the Scattering Matrix Elements Used

Here, we describe in detail how the different scattering processes are included in the formalism. The alloy scattering matrix elements are evaluated to describe the procedure of these calculations, and then the other scattering mechanisms are shown for completeness. These can be derived by the interested reader in the spirit of [34] with only minor changes with respect to the formalism presented here.

A. Elastic Scattering

Alloy scattering is treated here as the disturbing potential arising from alternating one of the atoms in a binary alloy, and the treatment follows [62]. The strength of this potential will depend on the mixing parameter x and the difference in the conduction-band edge ΔV between the compounds with $x = 0$ and $x = 1$. The potential from one fluctuating species located at $\vec{r}_i = \mathbf{r}_i + z_i\vec{e}_z$ is given by

$$V^i(\vec{r}) = C^x_i\,\delta(\vec{r}-\vec{r}_i)$$

where C^x_i is a random variable such that

$$\langle C^x_i\rangle_{\mathrm{alloy}} = 0$$
$$\langle C^x_i C^x_j\rangle_{\mathrm{alloy}} = \delta_{ij}x(1-x)(\Delta V V_{\mathrm{mol}})^2$$

and V_{mol} is the volume of one dimer (i.e., a fourth of the cubic unit cell for zincblende lattices). These properties determine the averages for the matrix elements in our basis, which read

$$\langle V^i_{\alpha\mathbf{k}_\alpha,\beta\mathbf{k}_\beta}V^j_{\gamma\mathbf{k}_\gamma,\delta\mathbf{k}_\delta}\rangle_{\mathrm{alloy}} = \frac{\delta_{ij}x(1-x)(\Delta V V_{\mathrm{mol}})^2}{A^2} \times\varphi^*_\alpha(z_i)\varphi_\beta(z_i)\varphi^*_\gamma(z_i)\varphi_\delta(z_i)\mathrm{e}^{-\mathbf{i}(\mathbf{k}_\alpha-\mathbf{k}_\beta+\mathbf{k}_\gamma-\mathbf{k}_\delta)\cdot\mathbf{r}_i} \quad (24)$$

showing that this is a local scattering process. Summing over all unit cells, effectively turning the sum into an integral

$$\sum_i \to \frac{1}{V_{\mathrm{mol}}}\mathrm{d}^3r_i$$

gives

$$\langle V^i_{\alpha\mathbf{k}_\alpha,\beta\mathbf{k}_\beta}V^j_{\gamma\mathbf{k}_\gamma,\delta\mathbf{k}_\delta}\rangle_{\mathrm{alloy}} = \frac{V_{\mathrm{mol}}}{A}\delta_{\mathbf{k}_\alpha-\mathbf{k}_\beta,\mathbf{k}_\delta-\mathbf{k}_\gamma}\int\mathrm{d}z\,\varphi^*_\alpha(z)\varphi_\beta(z)\varphi^*_\gamma(z)\varphi_\delta(z) \times x(z)(1-x(z))\Delta V^2(z) \quad (25)$$

which provides us with the squared matrix element used in (19) for the alloy scattering. The ϕ-integral provides a factor of 2π giving the final expression

$$X_{\alpha\alpha',\beta\beta'} = \frac{V_{\mathrm{mol}}m^*}{2\pi\hbar^2}\int\mathrm{d}z\,\varphi^*_\alpha(z)\varphi_\beta(z)\varphi^*_{\beta'}(z)\varphi_{\alpha'}(z) \times x(z)(1-x(z))\Delta V^2(z). \quad (26)$$

Now we proceed with the tensors for the other elastic scattering matrix elements. For interface roughness scattering, we assume the correlation functions

$$\langle \xi_i(\mathbf{r})\rangle = 0 \quad \langle \xi_i(\mathbf{r})\xi_j(\mathbf{r}')\rangle = \delta_{ij}\eta^2 \mathrm{e}^{-|\mathbf{r}-\mathbf{r}'|/\lambda_i}$$

for the deviation $\xi_i(\mathbf{r})$ of the interface i from its nominal position. Here, η is the average (RMS) height of the interface roughness and λ lateral correlation. Then, we obtain approximately (analogously to [34, Appendix B])

$$X^{\mathrm{rough}}_{\alpha\alpha'\beta\beta'}(E_k, E_{k'}) = \sum_j \frac{\Delta E_c^2 \eta_j^2}{2E_{\lambda_j}} \frac{1}{(a_j - b_j)\sqrt{a_j + b_j}} \times \varphi^*_\alpha(z_j)\varphi_\beta(z_j)\varphi^*_{\beta'}(z_j)\varphi_{\alpha'}(z_j) \quad (27)$$

where

$$a = 1 + \frac{E_k + E_{k'}}{E_\lambda} \qquad b = 2\frac{\sqrt{E_k E_{k'}}}{E_\lambda}$$

ΔE_c is the conduction band offset in energy, η is the average (RMS) height of the interface roughness, and $E_\lambda = \hbar^2/2m^*\lambda^2$.

Scattering at ionized dopants is treated as scattering from a number of delta-doping layers at positions z_i and areal density N^i_{2D}:

$$X^{\mathrm{imp}}_{\alpha\alpha',\beta\beta'}(E_k, E_{k'}) = \sum_i N^i_{2D} \frac{e^4}{16\pi\epsilon_s^2\epsilon_0^2} \frac{1}{2\pi}\int_0^{2\pi} \mathrm{d}\phi \left\{ \frac{1}{E_k + E_{k'} - 2\sqrt{E_k E_{k'}}\cos\phi + E_\lambda} \times \int \mathrm{d}z_1\, \varphi^*_\alpha(z_1)\varphi_\beta(z_1) e^{-q(\phi)|z_1 - z_i|} \times \int \mathrm{d}z_2\, \varphi^*_{\beta'}(z_2)\varphi_{\alpha'}(z_2) e^{-q(\phi)|z_2 - z_i|} \right\}$$

where $\hbar^2 q^2(\phi)/2m^* = E_k + E_{k'} - 2\sqrt{E_k E_{k'}}\cos\phi + E_\lambda$ and $E_\lambda = \hbar^2\lambda^2/2m^*$. The inverse screening length λ is determined by an interpolation between Debye and Tomas–Fermi screening for the average 3-D electron density. Even for very inhomogeneous distributions of the electrons along the period, this approximation is good as long as $\lambda d \lesssim 1$ [63].

B. Inelastic Scattering

In our current implementation, inelastic scattering processes are only due to the phonons. For the longitudinal optical phonons, we assume a constant frequency ω_{LO}. We consider the perturbation potential for the electron due to phonons with wave vector $\vec{q} = \mathbf{q} + q_z\vec{e}_z$:

$$V_{\mathrm{phon}}(\vec{r}, t) = \sum_{\mathbf{q}q_z} g(\vec{q})\mathrm{e}^{\mathrm{i}\mathbf{q}\cdot\mathbf{r} + \mathrm{i}q_z z}\left[b(\vec{q}, t) + b^\dagger(-\vec{q}, t)\right] \quad (28)$$

where $b(\vec{q}, t)$ and $b^\dagger(\vec{q}, t)$ are the bosonic annihilation and creation operators in the Heisenberg picture. For the polar interaction of the longitudinal optical phonons, we have the standard expression

$$|g(\vec{q})|^2 = g(\vec{q})g(-\vec{q}) = \frac{1}{AL}\frac{e^2}{|\vec{q}|^2}\frac{\hbar\omega_{LO}}{2\epsilon_0}\left(\frac{1}{\epsilon(\infty)} - \frac{1}{\epsilon(0)}\right)$$

where L is the normalization length for the phonons in the z-direction. Essentially following [44] and [64], we find in Born approximation (see also [54, Section IV.1.2])

$$\Sigma^<_{\alpha\alpha'}(E, \mathbf{k}) = \sum_{\beta\beta'}\sum_{q_z\,\mathbf{q}} |g(\vec{q})|^2 M_{\alpha\beta}(q_z)M_{\beta'\alpha'}(-q_z) \times \Big[G^<_{\beta\beta'}(E - \hbar\omega_{\mathrm{LO}}, \mathbf{k} - \mathbf{q})n_B + G^<_{\beta\beta'}(E + \hbar\omega_{\mathrm{LO}}, \mathbf{k} - \mathbf{q})(n_B + 1)\Big]$$

where n_B is the Bose distribution for the optical phonons at lattice temperature and

$$M_{\alpha\beta}(q_z) = \int \mathrm{d}z\, \varphi^*_\alpha(z)\mathrm{e}^{\mathrm{i}q_z z}\varphi_\beta(z).$$

The retarded self-energy reads

$$\Sigma^r_{\alpha\alpha'}(E, \mathbf{k}) = \sum_{\beta\beta'}\sum_{q_z\,\mathbf{q}} |g(\vec{q})|^2 M_{\alpha\beta}(q_z)M_{\beta'\alpha'}(-q_z) \times \Big[G^r_{\beta\beta'}(E - \hbar\omega_{\mathrm{LO}}, \mathbf{k} - \mathbf{q})(n_B + 1) + G^r_{\beta\beta'}(E + \hbar\omega_{\mathrm{LO}}, \mathbf{k} - \mathbf{q})n_B + \frac{1}{2}G^<_{\beta\beta'}(E - \hbar\omega_{\mathrm{LO}}, \mathbf{k} - \mathbf{q}) - \frac{1}{2}G^<_{\beta\beta'}(E + \hbar\omega_{\mathrm{LO}}, \mathbf{k} - \mathbf{q})\Big]$$

where a term containing a principal value integral [(127) of [54]] has been neglected. Using the fact that the Green's functions and self-energies do only depend on $|\mathbf{k}|$, the individual terms can be rewritten in the form

$$\Sigma_{\alpha\alpha'}(E, E_k) = \sum_{\beta\beta'}\int_0^\infty \mathrm{d}E_{k'} X^{\mathrm{opt}}_{\alpha\alpha'\beta\beta'}(E_k, E_{k'}) \times G_{\beta\beta'}(E \pm \hbar\omega_{\mathrm{LO}}, E_{k'}) \times [n_B \text{ or } (n_B + 1)] \quad (29)$$

with

$$X^{\mathrm{opt}}_{\alpha\alpha',\beta\beta'}(E_k, E_{k'}) = \frac{e^2\hbar\omega_{LO}}{16\pi^2\epsilon_0}\left(\frac{1}{\epsilon(\infty)} - \frac{1}{\epsilon(0)}\right) \times \int \mathrm{d}q_z \frac{M_{\alpha\beta}(q_z)M_{\beta'\alpha'}(-q_z)}{\sqrt{(\hbar^2 q_z^2/2m + E_k + E_{k'})^2 - 4E_k E_{k'}}}. \quad (30)$$

As in the elastic case, we apply the constant k approximation setting $E_k \approx E - (E_\alpha + E_{\alpha'})/2 = E_{\mathrm{typ}}$ and $E_{k'} \approx E \pm \hbar\omega_{\mathrm{LO}} - (E_\beta + E_{\beta'})/2 = E'_{\mathrm{typ}}$ in the Green's functions with the corresponding energy argument $E \pm \hbar\omega_{\mathrm{LO}}$. Again, the typical energy E is chosen such that $\mathrm{Min}\{E_{\mathrm{typ}}, E'_{\mathrm{typ}}\} = 1\mathrm{meV} + 0.3k_BT$.

For the deformation potential scattering with longitudinal acoustic phonons, we have

$$|g(\vec{q})|^2 = \Xi_c^2\frac{\hbar\omega(\vec{q})}{2\rho_m AL c_L^2}$$

in (28), where Ξ_c is the deformation potential of the conductance band, ρ_m is the mass density of the crystal, and c_L is

the longitudinal sound velocity. In general, these matrix elements are much smaller than the ones for optical phonon scattering or impurity scattering. However, we want to take acoustic phonons into account at least phenomenologically, so that there is some energy dissipation if optical phonon emission is energetically not allowed for. We make the essential simplifications to set $\hbar\omega(\vec{q}) \to \hbar\omega_{\rm ac} = k_B T$ in the energy arguments of the Green's functions and $n_B(\vec{q}) \to n_B(\hbar\omega_{\rm ac}) * \hbar\omega_{\rm ac}/\hbar\omega(\vec{q})$ as well as $n_B(\vec{q}) + 1 \to (n_B(\hbar\omega_{\rm ac}) + 1) * \hbar\omega_{\rm ac}/\hbar\omega(\vec{q})$ to mimic the q dependence of the occupation functions. This prefactor actually cancels with $\omega(\vec{q})$ in $|g(\vec{q})|^2$ and we find an expression completely analogously to (29) with

$$X^{\rm ac}_{\alpha\alpha'\beta'\beta} = \hbar\omega_{\rm ac}\frac{\Xi_c^2 m_e m^*}{4\pi\hbar^2\rho_m c_L^2}\frac{1}{L}\sum_{q_z} M_{\alpha\beta}(q_z)M_{\beta'\alpha'}(-q_z). \tag{31}$$

This expression does not depend on E_k and $E_{k'}$, so the constant k approximation is already included in the aforementioned approximations.

ACKNOWLEDGMENT

The authors would like to thank S.-C. Lee and R. Nelander for their earlier contributions to the model development.

REFERENCES

[1] J. Faist, F. Capasso, D. L. Sivco, C. Sirtori, A. L. Hutchinson, and A. Y. Cho, "Quantum cascade laser," *Science*, vol. 264, pp. 553–556, 1994.

[2] R. F. Curl, F. Capasso, C. Gmachl, A. A. Kosterev, B. McManus, R. Lewicki, M. Pusharsky, G. Wysocki, and F. K. Tittel, "Quantum cascade lasers in chemical physics," *Chem. Phys. Lett.*, vol. 487, pp. 1–18, 2010.

[3] A. Müller and J. Faist, "The quantum cascade laser: Ready for take-off," *Nat. Photon.*, vol. 4, p. 291, 2010.

[4] F. Capasso, "High-performance midinfrared quantum cascade lasers," *Opt. Eng.*, vol. 49, 111102 (9 pp.), 2010.

[5] R. Köhler, A. Tredicucci, F. Beltram, H. E. Beere, E. H. Linfield, A. G. Davies, D. A. Ritchie, R. C. Iotti, and F. Rossi, "Terahertz semiconductor-heterostructure laser," *Nature*, vol. 417, pp. 156–159, 2002.

[6] J. Darmo, V. Tamosiunas, G. Fasching, J. Kröll, K. Unterrainer, M. Beck, M. Giovannini, J. Faist, C. Kremser, and P. Debbage, "Imaging with a terahertz quantum cascade laser," *Opt. Exp.*, vol. 12, pp. 1879–1884, 2004.

[7] H.-W. Hübers, S. G. Pavlov, H. Richter, A. D. Semenov, L. Mahler, A. Tredicucci, H. E. Beere, and D. A. Ritchie, "High-resolution gas phase spectroscopy with a distributed feedback terahertz quantum cascade laser," *Appl. Phys. Lett.*, vol. 89, 061115 (3 pp.), 2006.

[8] B. S. Williams, "Terahertz quantum-cascade lasers," *Nature Phot.*, vol. 1, pp. 517–525, 2007.

[9] M. Lee and M. C. Wanke, "APPLIED PHYSICS: Searching for a solid-state terahertz technology," *Science*, vol. 316, pp. 64–65, 2007.

[10] M. Periera and O. Shulika, Eds., *Terahertz and Mid Infrared Radiatio*. (NATO Science for Peace and Security Series B Physics and Biophysics):. Dordrecht, The Netherlands: Springer-Verlag, 2011.

[11] F. Capasso, J. Faist, and C. Sirtori, "Mesoscopic phenomena in semiconductor nanostructures by quantum design," *J. Math. Phys.*, vol. 37, pp. 4775–4792, 1996.

[12] D. Paulavičius, V. Mitin, and M. A. Stroscio, "Hot-optical-phonon effects on electron relaxation in an AlGaAs/GaAs quantum cascade laser structure," *J. Appl. Phys.*, vol. 84, pp. 3459–3466, 1998.

[13] S. Slivken, V. I. Litvinov, M. Razeghi, and J. R. Meyer, "Relaxation kinetics in quantum cascade lasers," *J. Appl. Phys.*, vol. 85, pp. 665–671, 1999.

[14] P. Hyldgaard and J. W. Wilkins, "Electron–electron scattering in far-infrared quantum cascade lasers," *Phys. Rev. B*, vol. 53, pp. 6889–6892, 1996.

[15] P. Harrison, "The nature of the electron distribution functions in quantum cascade lasers," *Appl. Phys. Lett.*, vol. 75, pp. 2800–2802, 1999.

[16] C. Becker, C. Sirtori, H. Page, A. Robertson, V. Ortiz, and X. Marcadet, "Influence of confined phonon modes on the thermal behavior of AlAs/GaAs quantum cascade structures," *Phys. Rev. B*, vol. 65, 085305 (4 pp.), 2002.

[17] F. Compagnone, A. Di Carlo, and P. Lugli, "Monte Carlo simulation of electron dynamics in superlattice quantum cascade lasers," *Appl. Phys. Lett.*, vol. 80, pp. 920–922, 2002.

[18] K. Donovan, P. Harrison, and R. W. Kelsall, "Comparison of the quantum efficiencies of interwell and intrawell radiative transitions in quantum cascade lasers," *Appl. Phys. Lett.*, vol. 75, pp. 1999–2001, 1999.

[19] D. Indjin, P. Harrison, R. W. Kelsall, and Z. Ikonic, "Self-consistent scattering theory of transport and output characteristics of quantum cascade lasers," *J. Appl. Phys.*, vol. 91, pp. 9019–9026, 2002.

[20] S. Tortora, F. Compagnone, A. Di Carlo, P. Lugli, M. T. Pellegrini, M. Troccoli, and G. Scamarcio, "Theoretical study and simulation of electron dynamics in quantum cascade lasers," *Physica B*, vol. 272, pp. 219–222, 1999.

[21] R. C. Iotti and F. Rossi, "Carrier thermalization versus phonon-assisted relaxation in quantum cascade lasers: A Monte Carlo approach," *Appl. Phys. Lett.*, vol. 78, pp. 2902–2904, 2001.

[22] C. Jirauschek, G. Scarpa, P. Lugli, M. S. Vitiello, and G. Scamarcio, "Comparative analysis of resonant phonon THz quantum cascade lasers," *J. Appl. Phys.*, vol. 101, 086109 (3 pp.), 2007.

[23] O. Bonno, J. Thobel, and F. Dessenne, "Modeling of electron–electron scattering in Monte Carlo simulation of quantum cascade lasers," *J. Appl. Phys.*, vol. 97, 043702 (7 pp.), 2005.

[24] R. C. Iotti and F. Rossi, "Nature of charge transport in quantum-cascade lasers," *Phys. Rev. Lett.*, vol. 87, 146603 (4 pp.), 2001.

[25] H. Callebaut, S. Kumar, B. S. Williams, Q. Hu, and J. L. Reno, "Importance of electron-impurity scattering for electron transport in terahertz quantum-cascade lasers," *Appl. Phys. Lett.*, vol. 84, pp. 645–647, 2004.

[26] H. Callebaut and Q. Hu, "Importance of coherence for electron transport in terahertz quantum cascade lasers," *J. Appl. Phys.*, vol. 98, 104505 (11 pp.), 2005.

[27] C. Weber, A. Wacker, and A. Knorr, "Density-matrix theory of the optical dynamics and transport in quantum cascade structures: The role of coherence," *Phys. Rev. B*, vol. 79, 165322 (14 pp.), 2009.

[28] S. Kumar and Q. Hu, "Coherence of resonant-tunneling transport in terahertz quantum-cascade lasers," *Phys. Rev. B*, vol. 80, 245316 (14 pp.), 2009.

[29] E. Dupont, S. Fathololoumi, and H. C. Liu, "Simplified density-matrix model applied to three-well terahertz quantum cascade lasers," *Phys. Rev. B*, vol. 81, 205311 (18 pp.), May 2010.

[30] R. Terazzi and J. Faist, "A density matrix model of transport and radiation in quantum cascade lasers," *New J. Phys.*, vol. 12, 033045 (10 pp.), 2010.

[31] I. Waldmueller, W. W. Chow, E. W. Young, and M. C. Wanke, "Nonequilibrium many-body theory of intersubband lasers," *IEEE J. Quantum Electron.*, vol. 42, no. 3, pp. 292–301, Mar. 2006.

[32] A. Gordon and D. Majer, "Coherent transport in semiconductor heterostructures: A phenomenological approach," *Phys. Rev. B*, vol. 80, 195317 (6 pp.), 2009.

[33] A. Wacker, "Gain in quantum cascade lasers and superlattices: A quantum transport theory," *Phys. Rev. B*, vol. 66, 085326 (7 pp.), 2002.

[34] S.-C. Lee and A. Wacker, "Nonequilibrium Green's function theory for transport and gain properties of quantum cascade structures," *Phys. Rev. B*, vol. 66, 245314 (18 pp.), 2002.

[35] S.-C. Lee, F. Banit, M. Woerner, and A. Wacker, "Quantum mechanical wavepacket transport in quantum cascade laser structures," *Phys. Rev. B*, vol. 73, 245320 (6 pp.), 2006.

[36] T. Schmielau and M. Pereira, "Nonequilibrium many body theory for quantum transport in terahertz quantum cascade lasers," *Appl. Phys. Lett.*, vol. 95, 231111 (3 pp.), 2009.

[37] T. Kubis, C. Yeh, P. Vogl, A. Benz, G. Fasching, and C. Deutsch, "Theory of nonequilibrium quantum transport and energy dissipation in terahertz quantum cascade lasers," *Phys. Rev. B*, vol. 79, 195323 (10 pp.), 2009.

[38] G. Haldaś, A. Kolek, and I. Tralle, "Modeling of mid-infrared quantum cascade laser by means of nonequilibrium Green's functions," *IEEE J. Quantum Electron.*, vol. 47, no. 6, pp. 878–885, Jun. 2011.

[39] D. O. Winge, M. Lindskog, and A. Wacker, "Nonlinear response of quantum cascade structures," *Appl. Phys. Lett.*, vol. 101, 211113 (4 pp.), 2012.

[40] A. Wacker, "Coherence and spatial resolution of transport in quantum cascade lasers," *Phys. Stat. Sol. (c)*, vol. 5, pp. 215–220, 2008.

[41] H.-P. Breuer and F. Petruccione, *Open Quantum Systems*. Oxford, U.K.: Oxford Univ. Press, 2006.
[42] L. P. Kadanoff and G. Baym, *Quantum Statistical Mechanics*. New York, USA: Benjamin, 1962.
[43] L. V. Keldysh, "Diagram technique for nonequilibrium processes," *Sov. Phys. JETP*, vol. 20, p. 1018–1026, 1965 [Zh. Eksp. Theor. Fiz. **47**, 1515 (1964)].
[44] H. Haug and A.-P. Jauho, *Quantum Kinetics in Transport and Optics of Semiconductors*. Berlin, Germany: Springer-Verlag, 1996.
[45] A. Kolek, G. Haldaś, and M. Bugajski, "Nonthermal carrier distributions in the subbands of 2-phonon resonance mid-infrared quantum cascade laser," *Appl. Phys. Lett.*, vol. 101, 061110 (4 pp.), 2012.
[46] T. Schmielau and M. F. Pereira, "Impact of momentum dependent matrix elements on scattering effects in quantum cascade lasers," *Phys. Stat. Sol. (b)*, vol. 246, pp. 329–331, 2009.
[47] T. Kubis and P. Vogl, "Assessment of approximations in nonequilibrium Green's function theory," *Phys. Rev. B*, vol. 83, 195304 (12 pp.), May 2011.
[48] C. Ndebeka-Bandou, F. Carosella, R. Ferreira, A. Wacker, and G. Bastard, "Relevance of intra- and inter-subband scattering on the absorption in heterostructures," *Appl. Phys. Lett.*, vol. 101, 191104 (4 pp.), 2012.
[49] V. Eyert, "A comparative study on methods for convergence acceleration of iterative vector sequences," *J. Comp. Phys.*, vol. 124, pp. 271–285, 1996.
[50] F. Klappenberger, K. F. Renk, P. Renk, B. Rieder, Y. I. Koshurinov, D. G. Pavelev, V. Ustinov, A. Zhukov, N. Maleev, and A. Vasilyev, "Semiconductor–superlattice frequency multiplier for generation of submillimeter waves," *Appl. Phys. Lett.*, vol. 84, pp. 3924–3926, 2004.
[51] L. Esaki and R. Tsu, "Superlattice and negative differential conductivity in semiconductors," *IBM J. Res. Develop.*, vol. 14, pp. 61–65, 1970.
[52] A. Wacker and A.-P. Jauho, "Quantum transport: The link between standard approaches in superlattices," *Phys. Rev. Lett.*, vol. 80, pp. 369–372, 1998.
[53] A. A. Ignatov and Y. A. Romanov, "Nonlinear electromagnetic properties of semiconductors with a superlattice," *Phys. Stat. Sol. (b)*, vol. 73, pp. 327–333, 1976.
[54] A. Wacker, "Semiconductor superlattices: A model system for nonlinear transport," *Phys. Rep.*, vol. 357, pp. 1–111, 2002.
[55] D. H. Dunlap and V. M. Kenkre, "Dynamic localization of a charged particle moving under the influence of an electric field," *Phys. Rev. B*, vol. 34, pp. 3625–3633, 1986.
[56] G. Scalari, M. I. Amanti, C. Walther, R. Terazzi, M. Beck, and J. Faist, "Broadband THz lasing from a photon-phonon quantum cascade structure," *Opt. Exp.*, vol. 18, pp. 8043–8052, 2010.
[57] M. Helm, W. Hilber, T. Fromherz, F. M. Peeters, K. Alavi, and R. N. Pathak, "Infrared absorption in superlattices: A probe of the miniband dispersion and the structure of the impurity band," *Phys. Rev. B*, vol. 48, pp. 1601–1606, 1993.
[58] A. Wacker, G. Bastard, F. Carosella, R. Ferreira, and E. Dupont, "Unraveling of free-carrier absorption for terahertz radiation in heterostructures," *Phys. Rev. B*, vol. 84, 205319 (6 pp.), 2011.
[59] D. Burghoff, T.-Y. Kao, D. Ban, A. W. M. Lee, Q. Hu, and J. Reno, "A terahertz pulse emitter monolithically integrated with a quantum cascade laser," *Appl. Phys. Lett.*, vol. 98, 061112 (3 pp.), 2011.
[60] L. Gendron, M. Carras, A. Huynh, V. Ortiz, C. Koeniguer, and V. Berger, "Quantum cascade photodetector," *Appl. Phys. Lett.*, vol. 85, 2824 (3 pp.), 2004.
[61] L. Gendron, C. Kroeniguer, V. Berger, and X. Marcadet, "High resistance narrow band quantum cascade photodetectors," *Appl. Phys. Lett.*, vol. 86, 121116 (3 pp.), 2005.
[62] T. Ando, "Self-consistent result for a GaAs/Al_x Ga_{1-x} As heterojunction. ii. low temperature mobility," *J. Phys. Soc. Jpn.*, vol. 51, pp. 3900–3907, 1982.
[63] R. Nelander and A. Wacker, "Temperature dependence and screening models in quantum cascade structures," *J. Appl. Phys.*, vol. 106, 063115 (6 pp.), 2009.
[64] D. C. Langreth, "Linear and nonlinear response theory with applications," in *Linear and Nonlinear Electron Transport in Solids*, J. T. Devreese and V. E. van Doren, Eds. New York, USA: Plenum, 1976.
[65] T. Kubis and P. Vogl, "How periodic are quantum cascade lasers?" *J. Phys., Conf. Ser.* vol. 193, 012063 (4 pp.), 2009.
[66] T. Brandes, "Truncation method for Green's functions in time-dependent fields," *Phys. Rev. B*, vol. 56, pp. 1213–1224, 1997.

Andreas Wacker was born in Neuwied, Germany, and studied physics at RWTH Aachen. He received the Ph.D. degree from Technical University of Berlin, Berlin, Germany, under the supervision of Prof. E. Schöll.

After stays in Lyngby, Denmark, Madrid, Spain, and Berlin, he is currently a Professor for theoretical physics at Lund University, Lund, Sweden. His research focuses on nonequilibrium quantum transport in nanosystems.

Martin Lindskog was born in 1988 in Lund, Sweden. He received the Master of Science degree in physics from Lund University, Lund, in 2012, where he is currently working toward the Ph.D.degree at the Division of Mathematical Physics.

His work mainly focuses on simulation of quantum transport in quantum cascade structures.

David O. Winge was born in Lidhult, Sweden, 1987. He received the M.Sc. degree from Lund University, Lund, Sweden, in 2012, where he is currently working toward the Ph.D. degree at the Division of Mathematical Physics.

His research is in the field of quantum transport, especially in quantum cascade structures.